



HAL
open science

3D numerical simulation of seagrass movement under waves and currents with GPUSPH

Anne-Éléonore Paquier, Thibault Oudart, Caroline Le Bouteiller, Samuel Meulé, Philippe Larroudé, Robert Dalrymple

► **To cite this version:**

Anne-Éléonore Paquier, Thibault Oudart, Caroline Le Bouteiller, Samuel Meulé, Philippe Larroudé, et al.. 3D numerical simulation of seagrass movement under waves and currents with GPUSPH. International Journal of Sediment Research, 2021, 36 (6), pp.711-722. 10.1016/j.ijsrc.2020.08.003 . hal-02931623

HAL Id: hal-02931623

<https://hal.science/hal-02931623>

Submitted on 16 Oct 2023

HAL is a multi-disciplinary open access archive for the deposit and dissemination of scientific research documents, whether they are published or not. The documents may come from teaching and research institutions in France or abroad, or from public or private research centers.

L'archive ouverte pluridisciplinaire **HAL**, est destinée au dépôt et à la diffusion de documents scientifiques de niveau recherche, publiés ou non, émanant des établissements d'enseignement et de recherche français ou étrangers, des laboratoires publics ou privés.



Distributed under a Creative Commons Attribution - NonCommercial 4.0 International License

1

2 **3D Numerical simulation of seagrass movement under waves and**
3 **currents with GPUSPH**

4 Anne-Eléonore Paquier^{a,b}, Thibault Oudart^c, Caroline Le Bouteiller^d,
5 Samuel Meulé^b, Philippe Larroudé^{c*}, Robert A. Dalrymple^e

6 ^a*BRGM, Immeuble Agostini, Zone Industrielle de Furiani, 20600 Bastia*

7 ^b*Aix-Marseille University, CNRS, IRD, INRA, Coll France, CEREGE, Aix en Provence,*
8 *France*

9 ^c*Univerity Grenoble Alpes, Grenoble INP (Institute of Engineering), LEGI, 38000*
10 *Grenoble, France*

11 ^d*University Grenoble Alpes, IRSTEA, UR ETGR, F-38402 Saint-Martin-d'Herès,*
12 *France*

13 ^e*Department of Civil Engineering, Johns Hopkins University, Baltimore, MD, U.S.*

14 Corresponding author: Philippe Larroudé, LEGI, CS40700, 38058 Grenoble Cedex 9,
15 E-mail : philippe.larroude@legi.grenoble-inp.fr

16

17

18

19

20

21

22

23

24 **3D Numerical simulation of seagrass movement under waves and** 25 **currents with GPUSPH**

26 **Abstract**

27 The current study tries a new approach to simulating interactions between waves
28 and seagrass through Smoothed Particle Hydrodynamics (SPH). In this model,
29 the plants are defined as a solid that respects Hooke's law, and are assumed to
30 have direct interaction with the fluid. Given the characteristics of the SPH
31 method, especially in terms of computational time, the dimensions of the
32 simulations were limited. The first goal of the current study was to optimize the
33 approach to avoid reaching certain limits such as the rupture of the simulated
34 plant. Plant movements under waves and/or currents have been studied by several
35 authors in various *in-situ*, physical, and numerical experiments concerning
36 various vegetation species, thus, proving that plant movements can be
37 successfully reproduced by SPH 2D/3D. Manning's roughness coefficient, n , was
38 calculated to confirm that the results were in accordance with what had been
39 measured in flume studies. Even though there is still room for improvement, it is
40 shown that this method can be used to estimate Manning's coefficient for coastal
41 vegetation (seagrass and saltmarsh vegetation) and to greatly improve the
42 modeling and forecasting of coastal erosion and storm surge risks by including
43 the effect of vegetation in integrated models.

44 **Keywords:**

45 Numerical seagrass movement, GPUSPH, Fluid structure interaction, Waves,
46 Current

47

48 **1. Introduction**

49

50 Traditionally, to study fluid-structure interactions, structures usually are described with
51 a Lagrangian formulation while fluids often are represented through an Eulerian
52 formulation. The formulations generally are coupled using an Arbitrary Lagrangian-
53 Eulerian formulation for the fluid. Numerous fluid-structure interactions have been
54 studied according to such formulations, including valve springs (Rugonyi & Bathe,

55 2001), the interaction of compressible and incompressible fluids with structures (Bathe
56 & Zhang, 2004), and the absorption of hydro-elastic shocks (Le Tallec & Mouro, 2001).
57 The Lagrangian Smoothed Particle Hydrodynamics (SPH) method is a different
58 approach to modeling in which fluids and/or solids are represented by a set of particles.
59 Each solid particle has defined individual material properties and moves under the effect
60 of the fluid, itself represented by another set of particles. The use of a Lagrangian
61 formulation for fluids can be more convenient for certain types of applications, such as
62 fluid-free surface studies or large movements along a fluid-solid interface. Indeed, the
63 SPH method does not require specifically processing the fluid-free surface (no surface
64 tension) and the two groups of particles (fluid and solid) can be tracked simultaneously.
65 The SPH method has already been successfully used to study interactions between
66 fluids (Monaghan et al., 1999) and solids (Gotoh & Khayyer, 2018; Gray et al., 2001;
67 Liang et al., 2017; Van Liedekerke et al., 2013; Zhang et al., 2017).

68 The SPH method was developed in 1977 (Gingold & Monaghan, 1977; Lucy, 1977)
69 for applications in astrophysics. J. Monaghan (an Australian researcher in applied
70 mathematics) contributed greatly to the development of the method. Since 1985, the
71 method has been used for other applications. In the early 1990s, the SPH method was
72 used for fluid simulations including free surface flows, waves (Monaghan, 1994;
73 Randles & Libersky, 1996; Dalrymple & Rogers, 2006), multiphase fluids (Monaghan
74 & Kocharyan, 1995) and weakly compressible flows (Morris et al., 1997). In the field of
75 solid mechanics, simulations have mainly focused on the study of hypo-elastic solids
76 (Gray et al., 2001). Recent developments in science and engineering have increased the
77 need for modeling Fluid-Structure Interactions (FSI) to analyze multi-physics processes
78 like retroactive loops, in which the pressure and viscous stresses of the fluid create
79 deformation in the solid, which in turn affects stress, pressure, and velocity in the fluid.

80 Modeling FSI can, for instance, be useful for aerodynamics studies, biomechanics
81 simulations, or airbag design (Agamloh et al., 2008; Farhat et al., 2006). The earliest
82 models of stimulant-elastic solid and fluid interactions using the SPH method appeared
83 a little more than ten years ago and focused on the laws of interaction (Antoci et al.,
84 2007; Amini et al., 2011) and the definition of the solid interface (Ha et al., 2011). To
85 date, the SPH method has not often been applied to fluid-structure interactions in
86 environmental studies (Zhang et al., 2017). Here, it is proposed to use this method to
87 evaluate the influence of submerged aquatic vegetation on waves and currents in natural
88 hydrosystems.

89 Seagrasses form underwater meadows in the coastal zone. These meadows are
90 known to attenuate waves (Bradley & Houser, 2009; Fonseca & Cahalan, 1992; Koftis
91 et al., 2013; Paul & Amos, 2011; Kobayashi et al., 1993), and currents (Fonseca et al.,
92 1982; Fonseca & Fisher, 1986; Peterson et al., 2004; Widdows et al., 2008), and to
93 significantly influence sediment dynamics (Boscutti et al., 2015; Madsen et al., 2001).
94 Depending on the biometric characteristics of the species (shoot density, leaf area index,
95 plant stiffness, submergence ratio) and the morphological characteristics of the
96 meadows (extension, fragmentation), the effect on hydrodynamics will vary (Fonseca &
97 Koehl, 2006; Koftis et al., 2013; Paul & Amos, 2011; Stratigaki et al., 2011). The non-
98 linear interactions of these parameters with hydrodynamics variables (wave height,
99 wave period, water level, presence of a current) can also influence the attenuation of
100 waves, the modification of currents and sediment dynamics (Bradley & Houser, 2009;
101 Paquier et al., 2019; Paul & Amos, 2011).

102 Large-scale hydrosystem models can integrate the role of vegetation through a
103 change in the roughness coefficient. This can be done empirically through the
104 modification of Manning's n value (for example, in the ADCIRC model (Luettich et al.,

105 1992)). In other models, such as Xbeach (Roelvink et al., 2009) or Telemac (Hervouet,
106 2007), a specific vegetation roughness, as expressed by Mendez and Losada (2004), can
107 be used. The calculation of this parameter is based on the geometric and physical
108 characteristics of the vegetation meadow. This approach was very innovative in 2004,
109 and is now widely used in modeling. However, it does not account for vegetation
110 flexibility, which can be very important in subaquatic vegetation, especially when
111 canopies are sparse (Paquier et al., 2019). As seagrass meadows are declining around
112 the world (Waycott et al., 2009), it seems essential to better take into account vegetation
113 flexibility in hydrodynamics modeling and to better understand the role of declining
114 meadows or, more generally, sparse canopies. This could help to investigate seagrass
115 meadows' limitations as coastal buffers protecting against erosion and storm surges, and
116 could potentially enhance the protection of these declining ecosystems.

117 Sub-Aquatic Vegetation (SAV) is known to play a role in wave and storm surge
118 mitigation, and, thus, in coastal protection. The impacts of different species under
119 different conditions have already been studied (see introduction of Paquier et al. (2019)
120 for a review of the different processes observed). SAV has the ability to attenuate waves
121 and currents and to modify turbulence. However, no study to date has compared the
122 impacts of the different existing species. Such studies are nearly impossible to do in the
123 field considering the variety of environments in which the different species live.
124 Furthermore, experiments in flumes with real marine plants often are forbidden to
125 protect the marine plant species. A numerical study could, therefore, help remedy the
126 lack of *in-situ* studies. However, the modification in hydrodynamics generated by the
127 plants themselves is still difficult to estimate since plant movements under waves and
128 currents are still not well simulated and no exact numerical model exists (Mendez &
129 Losada, 2004; Sánchez-González et al., 2011). Generally, existing numerical studies use

130 rigid bodies to simulate plants with different roughness coefficients (Dalrymple et al.,
131 1984; Wallace & Cox, 2000). However, among the numerical studies dealing with
132 plants, Beudin et al. (2017) describe a three dimensional (3D) modeling framework that
133 simulates the interactions between waves, flow, and flexible vegetation. Beudin et al.
134 (2017) evaluated a plant drag model against field measurements in eelgrass canopies
135 and investigated the hydrodynamics in an idealized shallow-water setting.

136 The research presented herein aims to reproduce plant movement under waves and/or
137 current using the SPH method. The method was tested by building numerical two
138 dimensional (2D) and 3D flumes with the GPUSPH model (GPUSPH official website.
139 www.gpusph.org. Accessed: 2017-03-31.; Gómez-Gesteira et al., 2010; Hérault et al.,
140 2010, 2014), then comparing the simulations with the available data.

141 After a brief description of the SPH method (definition of the two numerical
142 approaches used for plants and water), several tests are presented of the FSI simulations
143 using the proposed model and these are compared with other simulations and with
144 experimental data (the FSI was calibrated and evaluated in the open source GPUSPH
145 code (Hérault et al., 2011).

146 The numerical simulation results are compared with experimental results based on
147 real or plastic seagrass meadows. The Young modulus is evaluated for real or fake
148 plants for both the experimental and numerical approaches. The wave attenuation due to
149 the seagrass meadow in the simulation also compared with experimental data. Finally, a
150 first simulation also is run with field data, collected in a bay occupied by a *Zostera*
151 *Noltei* meadow (another species of marine plant) in a large lagoon in Southern France.

152

153 **2. The SPH method and the FSI approach**

154

155 The SPH method is based on the theory of interpolation (Benz, 1990; Liu, 2002;
156 Monaghan, 1982; Monaghan, 1992; Monaghan, 2005). Its formulation often is divided
157 into two parts: (i) the integral representation, and (ii) the particle approximation. The
158 equation for the integral representation generally used in SPH is given in Appendix A.

159

160 *2.1. Equations for modeling the fluid*

161

162 The fluid was assumed to be only slightly compressible, isothermal, and governed by
163 the continuity equation:

$$164 \quad \frac{D\rho}{Dt} = -\rho \frac{\partial v_i}{\partial x_i} \quad (1)$$

165 and the motion equation:

$$166 \quad \rho \frac{Dv_i}{Dt} = \frac{\partial \sigma_{ij}}{\partial x_j} + \rho b_i \quad (2)$$

167 with $\frac{D}{Dt}$ defined by the material derivative:

$$168 \quad \frac{Du}{Dt} = \frac{\partial u}{\partial t} + v \cdot \nabla u \quad (3)$$

169 where ρ , v_i , σ_{ij} , and b_i are the density, velocity in i direction, stress tensor in ij
170 directions and force vector, respectively; t is time, x_i is the position in the i direction.

171 Stress tensor σ_{ij} is defined as:

$$172 \quad \sigma_{ij} = -p\delta_{ij} + S_{ij} \quad (4)$$

173 where p is pressure, δ_{ij} is the Kronecker tensor and S_{ij} is the deviatoric shear stress both
174 in the ij directions.

175

176 *2.2. Equations for modeling the solid*

177

178 The solids are governed by the same equations as the fluid. The stress tensor for a
 179 solid can similarly be decomposed into its isotropic pressure p and deviatoric shear
 180 stress S , as follows:

$$181 \quad \sigma_{ij} = -p\delta_{ij} + S_{ij} \quad (5)$$

182 where $p = -\sigma_{kk}/3$ is the isostatic pressure, δ_{ij} is the Kronecker tensor, and S_{ij} is the
 183 deviatoric shear stress (as for the fluid).

184 Equation 2 can, thus, be written as:

$$185 \quad \frac{Dv_i}{Dt} = \frac{1}{\rho} \frac{\partial S_{ij}}{\partial x_i} - \frac{1}{\rho} \frac{\partial p}{\partial x_i} + b_i \quad (6)$$

186 The linear relation that connects the stress and strain tensors can be derived from the
 187 time equation, S_{ij} . This is done by applying the Jaumann rate and gives the following
 188 corrected Hooke's law:

$$189 \quad \frac{DS_{ij}}{Dt} = 2\mu \left(D_{ij} - \frac{1}{3} D_{kk} \delta_{ij} \right) + S_{ik} \Omega_{jk} + \Omega_{ik} S_{kj} \quad (7)$$

190 where μ is the shear modulus, defined as:

$$191 \quad \mu = \frac{E}{2(1+\nu)} \quad (8)$$

192 and where E represents Young's modulus and ν represents Poisson's ratio. D_{ij} is the
 193 strain rate tensor:

$$194 \quad D_{ij} = \frac{1}{2} \left(\frac{\partial v_i}{\partial x_j} + \frac{\partial v_j}{\partial x_i} \right) \quad (9)$$

195 and Ω_{ij} is the rotation tensor:

$$196 \quad \Omega_{ij} = \frac{1}{2} \left(\frac{\partial v_i}{\partial x_j} - \frac{\partial v_j}{\partial x_i} \right) \quad (10)$$

197 In the case of large deformations, energy is not conserved. However, this method has
 198 the advantage of describing both the fluid and the solid dynamics in terms of pressure
 199 and velocity.

200 Pressure can be defined in the same way for both solids and fluid by applying the
 201 linearized equation of state:

$$202 \quad p = c_0^2(\rho - \rho_0) \quad (11)$$

203 with the speed of sound being $c_0 = \sqrt{\frac{\varepsilon}{\rho_0}}$ for the fluid and $c_0 = \sqrt{\frac{K}{\rho_0}}$ for the solids.

204 ε is the modulus of the fluid studied, ρ_0 a reference density, and K is the modulus of
 205 elasticity of the solid, which can be expressed as a function of Young's modulus, as
 206 follows:

$$207 \quad K = \frac{1}{3} \frac{E}{(1-2\nu)} \quad (12)$$

208

209

210 *2.3. Approximation of the motion equations through the SPH method*

211

212 *2.3.1. The fluid particles*

213

214 The following equation is obtained for the velocity of the fluid particles:

$$215 \quad \frac{Dv_{iq}}{Dt} = - \sum_b m_b \left(\frac{p_a}{\rho_a^2} + \frac{p_b}{\rho_b^2} \right) \delta_{ij} \nabla_a W_{ab} + g_i \quad (13)$$

216 with g_i = gravity, m_b the masse of the b particle, and the classical indices i, j, q, a,

217 and b of the SPH method .

218

219 *2.3.2. The solid particles*

220

221 The following equation is obtained for the velocity of the solid particles:

$$222 \quad \frac{Dv_{iq}}{Dt} = \sum_b m_b \left(\frac{S_{ija}}{\rho_a^2} + \frac{S_{ijb}}{\rho_b^2} - \left(\frac{p_a}{\rho_a^2} + \frac{p_b}{\rho_b^2} \right) \delta_{ij} \right) \cdot \nabla_a W_{ab} + g_i \quad (14)$$

223 However, Eq. 14 suffers from numerical instability and requires two terms to be
 224 introduced: one term for artificial viscosity and another term to correct tensile instability
 225 in the solid traction.

226 Artificial viscosity, Π_{ab} , was proposed by Monaghan (Monaghan & Gingold, 1983;
 227 Monaghan, 1992) and is used to smooth the oscillations caused by speed and to prevent
 228 the particles from being non-uniformly distributed in space when they are too close to
 229 each other.

$$230 \quad \frac{Dv_{ia}}{Dt} = \sum_b m_b \left(- \left(\frac{p_a}{\rho_a^2} + \frac{p_b}{\rho_b^2} \right) \delta_{ij} + \frac{S_{ija}}{\rho_a^2} + \frac{S_{ijb}}{\rho_b^2} + \Pi_{ab} \delta_{ij} \right) \cdot \frac{\partial W_{ab}}{\partial x_j} + g_i \quad (15)$$

$$231 \quad \Pi_{ab} \begin{cases} \frac{-\alpha c'_{ab} \mu_{ab}}{\rho'_{ab}} & v_{ab} r_{ab} < 0 \\ 0 & v_{ab} r_{ab} > 0 \end{cases} \quad (16)$$

232 with

$$233 \quad \mu_{ab} = \frac{h(v_{ab} r_{ab})}{|r_{ab}|^2 + 0.1h}, \quad r_{ab} = r_a - r_b, \quad v_{ab} = v_a - v_b, \quad c'_{ab} = \frac{1}{2}(c_a + c_b) \quad (\text{see Appendix$$

234 A).

235 This last term introduces a numerical dissipation, which must be minimized so as not to
 236 affect the solution. Antoci et al. (2007) proposed a compromise value between
 237 oscillation and dissipation.

238

239 *2.4. Correcting for speed*

240

241 To move the particles, the GPUSPH code uses the XSPH technique (Monaghan,
 242 1989). For each particle, a term containing the average speed of the surrounding
 243 particles is added to the original equation. Particle velocities, \vec{v} , were corrected
 244 according to the XSPH scheme to smooth out unwanted numerical peaks.

$$245 \quad \vec{v}_a = \vec{v}_a + \theta \frac{\sum_b \frac{m_b}{p_{ab}} (\vec{v}_b - \vec{v}_a) W_{ab}}{\sum_b \frac{m_b}{p_{ab}} W_{ab}} \quad (17)$$

246

247 The value of θ depends on the medium: $\theta = 0.08$ for the fluid which is increased to 1
248 to support high deformation for the solid.

249

250 2.5. Validation of solid elasticity

251

252 As proposed by Gray et al. (2001) and Antoci et al. (2007), the sensitivity of the
253 artificial viscosity and the XSPH factor can be tested by simulating the free oscillations
254 of an elastic plate having one end free and the other held in place. The plate is initially
255 horizontal (Fig. 1a) and an initial velocity distribution is assigned according to the
256 analytical expression of the free oscillations of a thin plate:

$$257 \quad v_z = v_{t0} c_0 \frac{f(x)}{f(L)} \quad (18)$$

258 where L is the length of the elastic plate and

$$259 \quad f(x) =$$

$$260 \quad (\cos(kL) + \cosh(kL))(\cosh(kx) - \cos(kx)) + (\sin(kL) - \sinh(kL))(\sinh(kx) -$$

261 $\sin(kx)) \quad (19)$

262 while $v_{t0} = 0.01$ determines the initial velocity of the free end and $kL = 1.875$ is the
263 fundamental mode. For a plate with the following features: $L = 0.2$ m, $H = 0.02$, m
264 $h = 0.2$ m, $\rho = 1000$ kg/m³, $K = 3.25 \times 10^6$ N/m², $\mu = 715000$ N/m², the analytical
265 non-dimensional amplitude (A) and period (T) of the first oscillation are $A/L = 0.115$
266 and $T c_0/L = 72.39$.

267 Gray et al. (2001) obtained $A/L=0.125$ and $T c_0/L = 82$ and Antoci et al. (2007)
268 obtained $A/L=0.124$ and $T c_0/L = 81.5$. For the proposed model the following was
269 obtained $A/L=0.116$ and $T c_0/L = 73.34$ (Fig. 2). The small difference between the
270 results can be attributed to several factors, but it's difficult to compare 2D simulations

271 and the current 3D simulations, since the mesh is different. The difference between the
272 current results and those presented by Antoci et al. (2007) and Gray et al. (2001)
273 probably come from the current use of 3D simulation.

274 As proposed by Antoci et al. (2007), this experiment allowed the artificial viscosity
275 coefficient, α , to be tested. In agreement with Antoci et al. (2007), the current numerical
276 experiment showed that if $\alpha = 0$, the simulation is unstable; when $\alpha > 1$ the free
277 oscillations damping reduces. Therefore, it was decided to use $\alpha = 1$, which caused
278 some slight energy dissipation but guaranteed good stability.

279 Monaghan (1992) proposed a tensile instability corrective formula specifically for
280 2D simulations, but which does not seem to be needed for 3D simulations. It can be
281 replaced by simply increasing the XSPH coefficient. For $0.5 < \theta < 2.5$, similar results
282 always were obtained. For simulations with higher initial velocities of the free end of
283 the plate ($v_{l0} = 0.05$ and $v_{l0} = 0.1$), good high oscillations without breakage were
284 obtained for $\theta = 1$ but the plate broke or become unstable for lower θ values (see Fig.
285 1b), and permanent deformations occurred for higher θ values.

286

287 *2.6. Fluid-Solid Interactions*

288

289 To simulate seagrass motion under waves and wave induced-currents, solid particles
290 must be defined to simulate the plants (a few millimetres thick) and the flume (a few
291 meters long). It was decided to create different particle sizes depending on the nature of
292 the element (water, interface, solid (see Fig. 1c)) and to adjust some interaction laws.

293 In order to use smaller particle sizes for the solid, interface particles were constructed
294 from the solid particles. They were then initialized with the sum of the masses of the
295 neighboring solid particles. The interface particles interact with the fluid particles

296 according to the different laws previously presented. The stresses on fluid particles are
297 directly transmitted to the interface particles, and for solid particles, the stresses are
298 transmitted proportionally to the mass ratio between the interface particles and the solid
299 particles. This treatment prevents a solid particle from being subjected to significant
300 stress due to its low mass. It also makes it possible to smooth and evenly distribute the
301 force on the solid particles.

302 Three different forces were tested to determine which one had the best fit for the current
303 simulations. The computational methods developed for FSI simulations with
304 deformable structures in the context of particle methods can be classified into several
305 categories, including FSI solvers. The latter were developed by coupling particle
306 methods with other computational methods or by integrating Lagrangian particles into
307 solvers for both the fluid and the solid. Several examples can be found in the reviews on
308 SPH methods done by Gotoh and Khayyer (2018) and Zhang et al. (2017).

309 Following Antoci et al. (2007), two types of boundary conditions were tested. First,
310 the Lennard-Jones boundary condition as used by Monaghan (2005) was tested. The
311 well-known Lennard-Jones formulation is a purely repulsive force principally used for
312 molecule interactions. The force, $f(r)$, per unit mass between a solid and a fluid particle
313 separated by a distance r has the form:

$$f(r) = D \left(\left(\frac{r_0}{r} \right)^{p_1} - \left(\frac{r_0}{r} \right)^{p_2} \right) \cdot \frac{r}{r_0} \text{ if } r > r_0$$

314
$$f(r) = 0 \text{ if } r \leq r_0 \tag{20}$$

315 The constants p_1 and p_2 (Eq. 20) must satisfy the condition $p_1 > p_2$ to be repulsive; we
316 set $p_1 = 12$ and $p_2 = 6$, were selected as proposed by Monaghan (1992).

317 The mass of an interface particle is calculated as the sum of the masses of the nearest
318 solid particles within its radius of action (a solid particle being bound to a single
319 interface particle). The interaction is then calculated between the interface particles and

320 the fluid particles, and the force calculated on the interface particles then is transmitted
321 to the linked solid particles, taking into account the mass ratios. The distance used in the
322 interaction laws between the interface particles and the fluid particles depends on the
323 size ratio between the interface particles and the solid particles at initialization so that
324 the interaction volume equals the volume of the solid particles.

325 Coefficient D depends on the water depth, H , and it is usually taken as $D = 5gH$. D is
326 applied to all the particles, and, therefore, does not generate any difference between
327 particle types.

328 A formulation proposed by Kajtar and Monaghan (2008) also was tested, i.e., the
329 same correction, as explained for (Eq. 20), was applied to the length scale. Both
330 boundary forces yielded similar results in the calculation of solid and fluid interactions.
331 Finally, the second boundary condition formulation that was tested concerned extending
332 the fluid and solid momentum and continuity equations to all particles regardless of
333 their nature. This formulation gave good results for the experiments of Antoci et al.
334 (2007). However, in cases with large differences in density between the fluid and the
335 solid, when impacts occurred, this formulation created local high pressure. Studies have
336 questioned or perfected these different approaches to boundary conditions (Crespo et
337 al., 2007; Ferrand et al., 2013). In the current case, the standard options in the GPUSPH
338 code worked well enough for the current needs.

339

340 **3. Calibration and comparison with experimental data**

341 Antoci et al. (2007) did a laboratory experiment and compared the results with SPH
342 simulations. The experiment consisted in deforming an elastic bundle acting as a dam in
343 a water column. The configuration of the experiment is described in Antoci et al.
344 (2007). Table 1 lists the size experiment parameters. The elastic properties of the beam

345 can be determined from Antoci et al. (2007). For the current simulations, a Young's
346 modulus that provided the results closest to the experimental results was chosen. Liquid
347 and elasticity properties are listed in Table 2.

348 To calibrate and validate the fluid-structure interaction (FSI) model used for plant
349 movement, the current results were compared for the vertical (Fig. 3a) and horizontal
350 movements (Fig. 3b) at the end of the plate with Antoci et al. (2007). The numerical
351 results are consistent with the experimental results found by Antoci et al. (2007).

352

353 A fluid compressibility below the theoretical value was used to reduce the time step,
354 as was done by Antoci et al. (2007). Despite this difference in compressibility, the
355 displacements obtained were within the expected range.

356 In the current study, the Lennard-Jones (Monaghan, 2005), and Kajtar and
357 Monaghan (2008) boundary conditions were used, and better results were found with
358 the latter formulation. The proposed multi-scale approach also was validated with Kajtar
359 and Monaghan (2008) boundary conditions for solid particles until they were ten times
360 closer together than the fluid particles and with an interface particle similar to the one
361 described in the previous section. A multi-scale approach such as this is needed to
362 simulate small elastic solids in a fluid domain.

363

364 **4. Results and discussion**

365

366 The plant movements predicted with the proposed SPH simulations were compared
367 with both experimental results (Le Bouteiller & Venditti, 2015; Luhar & Nepf, 2011)
368 and field observations (Paquier et al., 2019).

369 Different species of seagrass colonize the shallow coastal waters around the world,
370 often forming large underwater meadows. Seagrass meadows are known to reduce wave
371 height and current velocity near the seabed, but the simulation meadow (see Fig. 4),
372 could be also a problem for the simulations. The different datasets used for the current
373 comparisons were collected on real or mimicked plants of different species. Luhar and
374 Nepf (2011) and Stratigaki et al. (2011) worked on mimics of *Posidonia oceanica*, Le
375 Bouteiller and Venditti (2015) worked on mimics of *Zostera marina* and Paquier et al.
376 (2019) worked on real *Zostera noltei*.

377

378 4.1. Comparison using the initial 2D approach

379 The comparison was done on the basis of Luhar and Nepf's (2011) study. Plant
380 modeling relies on solid knowledge of the physical properties of the plant (height and
381 thickness but also density and elastic modulus). In addition, it is complicated to
382 numerically simulate a very thin leaf. For the species *Posidonia Oceanica*, Folkard
383 (2005) gives clear leaf properties (Table 3). Poisson's ratio is not given, but generally
384 ranges from 0.3 to 0.4 for this type of solid.

385 Several limitations were encountered during the simulation process of the *Posidonia*
386 *Oceanica* leaf thickness. First, the thickness of the plant leaf is naturally 0.1 mm and the
387 particle size used for the simulations was 5 mm (a ratio of 1/150). To deal with this
388 issue two choices were available: either divide the particle size by 150 or modify the
389 plant properties while conserving a comparable flexibility. The 2D code as used
390 originally (Oudart & Larroudé, 2012) does not accept multi-sized particles, which
391 would induce a decrease in the water particle size. Furthermore, reducing the particle
392 size would have dramatically increased the number of particles, and, thus, the
393 computation time. The memory needed to run such a calculation is much too large to

394 allow the use of the SPH method. Therefore it was decided to modify the plant
395 properties. Plant thickness, Young's modulus and fluid compressibility were modified.
396 The impact of density was not investigated; and another study should be done on this
397 point. The final modified parameters of the plants are listed in Table 3.

398 Some seagrass species' leaves (including *Posidonia Oceanica*) grow from shoots in
399 small groups (the number of leaves per shoot depends on the species and can vary from
400 one shoot to another). These shoots cannot be simulated in a 2D model. However,
401 several leaves close to each other were simulated in order to represent a natural meadow
402 as well as possible. Figure 5 shows the movement of three simulated leaves (as a first
403 approach to meadow simulation) under a breaking wave. The numerical representation
404 of the deformation of the plants in a meadow is therefore possible.

405 Luhar and Nepf (2011) did laboratory experiments to study the flow-induced
406 reconfiguration of flexible subaquatic vegetation. The plant mimics used were inspired
407 by *Posidonia Oceanica* plants; the drag and posture of the mimics were within the
408 natural range for stiffness and buoyancy. Luhar and Nepf (2011) then compared the
409 experimental results with a theoretical model. Two current velocities were tested: one
410 lower and one higher than the restoring forces, the latter flow bending the leaves. The
411 current simulation was compared to Luhar and Nepf's (2011) experiments from a
412 qualitative point of view. Luhar and Nepf (2011) built two kinds of leaves:

413 - one made of silicone foam (Young's modulus, $E = 500 \text{ kPa}$; $\Delta\rho = 330 \text{ kg/m}^3$ with a
414 seawater density assumed to be 1025 kg/m^3 ; thickness = 1.9 mm);

415 - one made of high-density polyethylene (HDPE) (Young's modulus, $E = 0.93 \text{ GPa}$;
416 $\Delta\rho = 50 \text{ kg/m}^3$; thickness = 0.4 mm).

417 Figure 6a shows Luhar and Nepf's (2011) experimental set up and the comparison
418 with the current simulations (Figs. 6b,c and Figs. 6d,e). For both current velocities, the

419 SPH simulation gives the correct inclination of the plant. For the low current velocity
420 ($U = 0.16$ m/s), an inclination angle of 45° was obtain versus 38° angle obtained in the
421 experiment with silicon foam leaf blades (see Figs. 6b,c).

422 For the higher current velocity ($U = 0.32$ m/s), Luhar and Nepf (2011) measured an
423 angle of 21° while an angle of 26° was simulated. The shape of the numerically
424 simulated blade is in reasonable agreement with the experimental results shown in black
425 on the picture (see Fig. 6e).

426 In the experiment, Luhar and Nepf (2011) also built artificial leaf blades from HDPE.
427 Again, the SPH simulation showed results similar to the experimental results. The
428 difference Luhar and Nepf (2011) observed in the angle taken for the HDPE leaf
429 compared to the silicon leaf is well represented by the SPH modeling.

430

431 *4.2. Comparing simulated 2D and 3D plant effects on waves with experimental*
432 *results*

433

434 The simulated 2D results were compared with the experimental results of Luhar and
435 Nepf (2011) and Stratigaki et al. (2011); both researchteams worked on *Posidonia*
436 *Oceanica* mimics. The simulated 3D results were compared with those of Paquier et al.
437 (2019), who worked in the field on real *Zostera noltei* plants (a smaller species than
438 *Posidonia Oceanica*).

439 The 3D modeling approach used in the current study allowed simulation of plant
440 movements under waves. The results for different h_0/h_{plant} ratios (where h_0 is the
441 reference water level in the channel and h_{plant} is the height of the plant) were compared
442 for one plant located at a distance of $x = 1.2$ m (Fig. 7) from the piston paddle. The
443 height of the wave generated by the piston paddle was influenced at $x = 0.6$ m from the

444 paddle. This boundary condition is too close to the seagrass meadow and the
445 computational domain had to be increased (Oudart & Larroudé, 2012; Oudart et al.,
446 2013).

447 The wave heights at $x = 1$ m and $x = 1.3$ m were nearly identical for all the
448 simulations: wave height increased at the approach to the plant and decreased
449 significantly afterwards. However, when approaching the area of the channel slope (at x
450 $= 1.7$ m), there was another increase in wave height, which varied according to the ratio
451 h_0/h_{plant} . The presence of the plant generated a decrease in the wave height at this
452 location, due to a loss of energy resulting from friction. Reflecting this situation
453 numerically would require complementary simulations with the foot of the beach slope
454 far from the end of the sea grass meadow to avoid any slope influence on wave
455 attenuation.

456 Different scenarios were simulated: a channel without plants (Case 0), with one
457 elastic plant (Case 1), with one rigid plant (Case 2), and with three elastic plants located
458 at $x = 1$ m, $x = 1.2$ m, $x = 1.4$ m from the wave maker (Case 3). Plant height was set at
459 0.1 meter ($h_0/h_{\text{plant}}=0.5$ m, $h_0 = 0.2$ m); the changes in wave height relative to h_0 along
460 the cross section is represented in Fig. 7. In the presence of a rigid plant (Case 2), wave
461 height decreased then increased again after the plant due to the recirculation generated
462 by the rigid obstacle. With a three-plant meadow (Case 3), the decrease in wave height
463 was higher than with a single plant (Case 2) and significantly higher than without any
464 plants (decrease 24% greater for Case 3 than for Case 0). Stratigaki et al. (2011)
465 observed a decrease of 30 to 35% in wave height in their experimental study. These
466 higher rates can be explained by a longer friction zone in the experiment than in the
467 numerical simulations shown in Fig. 7.

468 2D simulations were appropriate for comparison with some experimental studies
469 (Antoci et al., 2007; Luhar & Nepf, 2011; Stratigaki et al., 2011). These experiments are
470 consistent with a 2D approach because very little flow can pass on each side of the
471 seagrass. Indeed, the plant mimics in the foregoing studies were as wide as the channel
472 or the meadow took up the whole width of the experimental set up. Obviously, to
473 simulate experiments with sparser seagrass meadows or marine plants from coastal
474 zones other than the ones studied by Stratigaki et al. (2011) and Luhar and Nepf (2011),
475 a 3D simulation is necessary. The proposed multi-scale 3D FSI simulations with the
476 SPH method are able to reproduce the shape and phasing of leaf movements resulting
477 from the wave passing over the plant or plant meadow. This is the first step toward
478 developing a more quantitative approach. It also was possible to simulate this
479 movement for an entire 3D meadow of 200 plants (Fig. 8a) and for a 3D meadow with
480 two separate zones of seagrass (Fig. 8b).

481 With a 3D method, different particle sizes can be used for water and plants. This makes
482 it possible to (i) create plants with a more realistic thickness, (ii) to simulate several
483 plants (200 in the current case), and (iii) to simulate several densities of seagrass
484 meadow with realistic bathymetry (see Fig. 9). Fig. 9d shows the numerical results with
485 and without a plant meadow on a real bathymetry (the “Point de Berre” beach in Berre
486 Lagoon, France, (Paquier et al., 2019)). This first qualitative approach with the 3D SPH
487 method clearly shows the attenuation of the waves by the plants. The simulated plant
488 movements (Figs. 9a, b and c) are also qualitatively consistent with those observed in
489 the study area (video available in the supplementary material in Paquier et al. 2019).

490 The next research step will be to calibrate the model with in-situ wave measurements.
491

492 4.3. Comparison of simulated flow properties (Manning's coefficient) with
493 experimental results

494

495 The aim of the TEC21 post-doc program at the University of Grenoble was to
496 numerically reproduce the experiment of Le Bouteiller and Venditti (2015), which had
497 been done on mimics of *Zostera marina* in an inclined flume (15 m long and 1 m wide)
498 located in the River Dynamics Laboratory at Simon Fraser University in Canada (Figs.
499 10a,b). The central section of the flume between 5 and 11 m was covered with a
500 vegetated bed (see Fig. 10a) consisting of staggered artificial blades. The blades were
501 made of a low density polyethylene film (920 kg/m^3) with a Young's modulus of 2×10^8
502 Pa, a length of 25.5 cm, a width of 0.75 cm and a thickness of 0.2 mm (see Fig. 10b).
503 The material and dimensions of the blades were chosen for their similarity to natural
504 *Zostera marina* plants to maintain the ratio of flexural rigidity to buoyancy forces
505 (Ghisalberti & Nepf, 2002). Two densities of plants were used in the experiments: 130
506 blades (low density) and 800 blades (high density) per square meter.

507

508 To simulate the interactions between the low-density meadow and hydrodynamics,
509 several lines of plants were built. For the low-density meadow experiment, the lines
510 were 6.25 cm from each other and the plant mimics were spaced 12.5 cm apart on each
511 line. The alignment of the plants on one line was shifted by 6.25 cm from the previous
512 line to form an alternating network. The nearest surrounding plants were, therefore,
513 around 8.8 cm away. For the high-density meadow experiment, the lines were separated
514 by 2.5 cm while the plant mimics on each line were affixed every 5 cm. Again, an
515 alternating network was built. The nearest surrounding plants were, therefore, around
516 3.56 cm away. In the simulation presented here, the low-density meadow case was

517 considered (see Fig. 10c). The simulated movements of the plants correspond to what
518 was observed during the actual flume experiment (see Figs. 10b,c, and d), even if a
519 better quantitative evaluation of the simulated plants' movements is still needed. A
520 Manning's n coefficient similar to the one found experimentally by Le Bouteiller and
521 Venditti (2015) based on a uniform flow hypothesis was evaluated. For the low-density
522 meadow, Le Bouteiller and Venditti (2015) found a Manning's n coefficient value of
523 0.023, which remained constant under increasing flow velocity. In the current study, a
524 Manning's coefficient equal to 0.025 was obtained. A better parametrization of the
525 Manning's n evaluation is still needed but it does seem appropriate to use the GPUSPH
526 simulation to calculate the Manning's n coefficient. The evaluation of the Manning's n
527 following the SPH simulation gave good results for the mesh (number of particles) used
528 in the test cases. In future studies, the mesh should be increased to refine the results.
529 What is pointed out in the current study is that it is feasible to use the same Manning's n
530 evaluation methodology for 3D SPH simulations and real experiments.

531

532

533 **5. Conclusions**

534

535 The results obtained for the various FSI simulations with the SPH method were
536 reasonable, even though improvements can be made in the future. First, in a
537 deformation test case of an elastic plate under a column of water, it was shown that it is
538 possible to model the movement of a solid submitted to water effects with the SPH
539 method and FSI. Plant movements also were successfully simulated in a wave flume.
540 The different curves taken by the plant under the passing waves show the role of the
541 plant in wave height modification. In these initial simulations, the decrease in wave

542 height was significant. The influence of plant flexibility (in opposition to a rigid body)
543 also was investigated. Further numerical experiments are needed to include larger
544 and/or higher meadows that have been studied in physical experiments and in-situ in the
545 literature.

546 Current modeling limitations include the sizing problems of the particles related
547 to the cost in computation time but these limitations will undoubtedly be overcome in
548 the future. Even so, the SPH method is still time-consuming in terms of computation for
549 simulations over large areas. It is, however, a good way to evaluate an equivalent
550 viscosity that can be applied in other methods and models. Once wave damping *in-situ*
551 can be quantitatively simulated, researchers will be able to simulate the role of any plant
552 and to determine an equivalent viscosity depending on each plant's properties.
553 Improvements will likely be made to the methodology presented here for comparing
554 SPH models with existing experiments and the computational time required for 3D
555 calculations will tend to decrease with better computer technology. For the time being,
556 however, it is difficult to do quantitative comparisons between simulations and existing
557 experimental results due to the differences in the initial parameters themselves and to
558 the limitations of the SPH method (especially regarding computational time). The next
559 step in this research will be to build simpler theoretical cases (for which the
560 dimensioning of the elements and the quantification of the fluid and solid movements
561 are known) through SPH simulations and to evaluate the need to add a coefficient to the
562 law of interaction.

563

564 It was also possible to simulate long plastic blades with high flexibility based on the
565 experimental flume data from Le Bouteiller and Venditti (2015). This allowed a
566 Manning's n coefficient to be calculated consistent with the one experimentally

567 evaluated by Le Bouteiller and Venditti (2015). The next step in this study will be to
568 ensure the quantification of this numerical reproduction and to improve the accuracy of
569 the estimated Manning's n roughness coefficient for a variety of seagrass species. There
570 is a real need for these values for the coastal management community's use in integrated
571 models.

572 Interest in the role of nature-based defences is growing (Bridges et al., 2015;
573 "Committee on Environment", 2015) and model users must respond to this need. The
574 proposed method, applied to a wide range of vegetation species with various biometric
575 parameters, will make it possible to evaluate Manning's n for a great number of plants;
576 the proposed model, therefore, represents a breakthrough in modeling.

577 Another aspect of this research, within the framework of the CANOPÉ program, was
578 to do 3D SPH simulations based on *in-situ* measurements collected from three coastal
579 zones with seagrass meadows. This reflects another fundamental objective of the
580 present feasibility study of 3D sea-plant/wave interaction simulations: applications in
581 environmental engineering. Indeed, one future option in the context of coastal
582 protection is to use seagrass meadows as protective barriers, either by extending
583 existing seagrass beds or by creating artificial ones. In this case, large-scale digital
584 studies can supplement *in-situ* studies. Channel experiments cannot be set up with real,
585 often protected, marine plants; therefore, the authors hope that the virtual FSI channel
586 will contribute to solving these environmental objectives. Finally, a layer of sediment
587 (Ghaïtanellis et al., 2018) or gravel (Kazemi et al., 2020) could also be taken into
588 account, which, when added to the plant/wave interaction we simulated in our study,
589 would be able to numerically reproduce a complete coastal system.

590

591 **Acknowledgements**

592 The authors gratefully acknowledge the support of the NVIDIA Corporation who donated
593 the GTX 780 GPU used for this research. This research was partially supported by the LabEx
594 Tec 21 program (Investissement d’Avenir - grant agreement ANR-11-LABX-0030) and by
595 financial support from the “Agence de l’Eau RM&C” through the CANOPé research program.
596 AEP was partially supported by the French National Research Agency (ANR) through ANR
597 @RAction chair medLOC (ANR-14-ACHN-0007-01 – project leader Thomas Stieglitz). The
598 authors also thank M. Luhar and H. Nepf (from MIT) for the exchange of information and data.
599

600 APPENDIX A:

601 The integral representation of an arbitrary function, $F(r)$, is defined as follows:

$$602 \quad F(r) = \int_V F(r') \delta(r - r') dr' \quad (\text{A.1})$$

603 where $\delta(r - r')$ represents the Dirac delta function, V is the area of integration (in two
604 dimensions) and r is the position vector. For the SPH method an approximation to the
605 delta function is:

$$606 \quad F(r) \approx \int_V F(r') W(r - r', h) dr' \quad (\text{A.2})$$

607 where h is the smoothing length defined by the area of influence of the smoothing
608 function (or weight function), W .

609 In the SPH method, the system is represented by a number of particles, each carrying
610 a mass and other fluid parameters and defined in a specific area of space. The particle
611 approximation is used to discretize the domain. If $F(r')$ is known in N discrete points
612 r_1, r_2, \dots, r_N , then it can be approximated by:

$$613 \quad F_h(r) = \sum_{b=1}^N \frac{m_b}{\rho_b} F_b W(r - r', h) \quad (\text{A.3})$$

614 where b corresponds to a particle neighbor. The kernel function must satisfy (Benz,
615 1990; Liu, 2002; Monaghan, 1992):

$$616 \quad \left\{ \begin{array}{l} \int_V W(r - r', h) dr' = 1 \\ \lim_{h \rightarrow 0} W(r - r', h) = \delta(r - r') \\ W(r - r', h) = 0 \text{ when } |r - r'| > \kappa h \end{array} \right. \quad (\text{A.4})$$

617 The first condition is the *normalization condition*, the second is the *Delta function*
618 *property* (observed when the smoothing length approaches zero), and the third is the
619 *compact condition* where κ is a constant related to the length of smoothing and which
620 defines the effective area of the smoothing function.

621 The stability of the SPH algorithm depends heavily on the second derivative of the
622 kernel (Morris et al., 1997). There are different kernel functions, the most well-known
623 being a Gaussian function. In the current study, the Wendland function primarily was
624 used:

$$625 \quad W(r, h) = \frac{\Psi}{h^v} \begin{cases} 1 - 1.5s^2 + 0.75s^3 & 0 \leq s \leq 1 \\ 0.25(2 - s^3) & 1 \leq s \leq 2 \\ 0 & 2 \leq s \end{cases} \quad (\text{A.5})$$

626 where $s = \frac{|r|}{h}$, and Ψ is the normalization constant, equal to $10/7 \pi$ for two dimensions.

627 The accuracy of the SPH method can be improved by increasing the number of
628 neighbors considered, which also significantly increases computational time. In the case
629 of 2D modeling, a number of neighboring particles between 20 and 30 is a good
630 compromise between accuracy and computational time; this number needs to be
631 increased to 80 for 3D modeling.

632

633 There are two forms used to calculate a gradient of a scalar F in SPH. One is mainly
634 used when the particle density varies only slightly:

$$635 \quad \frac{1}{\rho_a} \nabla_a F = \sum_b m_b \left(\frac{F_a}{\rho_a^2} + \frac{F_b}{\rho_b^2} \right) \nabla_a W_{ab} \quad (\text{A.6})$$

636 where ∇_a represents the gradient of the particle and $\nabla_a W_{ab}$ is the gradient of the kernel
637 function $W(|r_a - r_b, h|)$ with r_a the coordinates of the particle a . The second form is as
638 follows:

$$639 \quad \nabla_a W_{ab} = \nabla_a W(r_a - r_b, h) = \frac{dW}{dr_{ab}} \frac{1}{|r_{ab}|} (x_a^\alpha - x_b^\beta) \quad (\text{A.7})$$

640 with $F_{ab} = F_a - F_b$, $r_{ab} = r_a - r_b$. More details about these two forms used to calculate
641 a gradient can be found in GPUSPH Theory Guide, version 5.0 (2016),
642 <https://www.gpusph.org/documentation/theory-guide/>.

643

644

645 References

646

647 Agamloh, E., Wallace, A., & Von Jouanne, A. (2008). Application of Fluid Structure
648 Interaction Simulation of an Ocean Wave Energy Extraction Device. *Renewable*
649 *Energy*, 33(4), 748-757. doi: 10.1016/j.renene.2007.04.010

650

651 Amini, Y., Emdad, H., & Farid, M. (2011). A new model to solve fluid–hypo-elastic
652 solid interaction using the smoothed particle hydrodynamics (SPH) method.
653 *European Journal of Mechanics B/Fluids*, 30, 184–194

654

655 Antoci, C., Gallati, M., & Sibilla, S. (2007). Numerical simulation of fluid–structure
656 interaction by SPH. *Computers and Structures*, 85, 879–890.

657

658 Bathe, K.J., & Zhang, H. (2004). Finite element developments for general fluid flows
659 with structural interactions. *Int. J. Numer. Meth. Engng*, 60, 213–232. doi:
660 10.1002/nme.959.

661

662 Beudin, A., Kalra, T.S., Ganju, N.K., & Warner, J.C. (2017). Development of a coupled
663 wave-flow-vegetation interaction model. *Computers & Geosciences*, 100, 76–86.

664

665 Benz, W. (1990) Smooth Particle Hydrodynamics: A Review. In: Buchler J.R. (eds) The
666 Numerical Modelling of Nonlinear Stellar Pulsations. NATO ASI Series (Series
667 C: Mathematical and Physical Sciences), 302. Springer, Dordrecht.
668

669 Boscutti, F., Marcorin, I., Sigura, M., Bressan, E., Tamberlich, F., Vianello, A., &
670 Casolo. (2015). Distribution modeling of seagrasses in brackish waters of
671 Grado-Marano lagoon (Northern Adriatic Sea). *Estuarine, Coastal and Shelf
672 Science* 164, 183-193. doi:10.1016/j.ecss.2015.07.035
673

674 Bradley, K., & Houser, C. (2009), Relative velocity of seagrass blades: Implications for
675 wave attenuation in low-energy environments, *J. Geophys. Res.*, 114, F01004,
676 doi: 10.1029/2007JF000951.

677 Bridges, T.S., Wagner, P.W., Burks-Copes, K.A., Bates, M., & Collier, Z.A. (2015).
678 *Use of natural and nature-based features (NNBF) for coastal resilience.* (Report
679 No. ERDC SR-15-1). USACE-ERDC
680

681 Committee on Environment, Natural, Resources, and Sustainability, National Science
682 and Technology Council. (2015). Ecosystem-service assessment: research needs
683 for coastal green infrastructure. Executive Office of the President of the United
684 States

685 Crespo, A.J., Gómez-Gesteira, M., & Dalrymple, R.A. (2007). Boundary Conditions
686 Generated by Dynamic Particles in SPH Methods, CMC. *Computers, Materials,
687 & Continua*, 5(3), 173-184.
688

689 Dalrymple, R.A., Kirby, J.T., & Hwang, P.A. (1984). Wave Diffraction Due to Areas of
690 Energy Dissipation. *Journal of Waterway, Port, Coastal, and Ocean*
691 *Engineering*, 110(1), 67-79.

692

693 Dalrymple, R.A., & Rogers, B.D. (2006). Numerical Modeling of Water Waves with
694 the SPH Method. *Coastal Engineering*, 53(2-3), 141-147.

695

696 Farhat, C., Van der Zee K., & Geuzaine P. (2006). Provable second-order time-accurate
697 loosely-coupled solution algorithms for transient nonlinear computational
698 aeroelasticity. *J. Comput. Methods Appl. Mech. Eng.*, 195, 1973–2001

699

700 Ferrand, M., Laurence, D., Rogers, B., Violeau, D., & Kassiotis, C. (2013). Unified
701 semi-analytical wall boundary conditions for inviscid, laminar or turbulent flows
702 in the meshless SPH method. *International Journal for Numerical Methods in*
703 *Fluids*, 71, 476-472. doi:10.1002/flid.3666

704

705 Fonseca, M.S. & Fisher, J.S. (1986). A comparison of canopy friction and sediment
706 movement between four species of seagrass with reference to their ecology and
707 restoration. *Marine Ecology Progress Series* 29, 15-22.

708

709 Fonseca, M. S., Fisher, J. S., Zieman, J. C., & Thayer, G.W. (1982). Influence of the
710 seagrass, *Zostera marina* L., on current flow. *Estuarine, Coastal and Shelf*
711 *Science* 15 (4), 351-358. doi:10.1016/0272-7714(82)90046-4

712 Fonseca, M. S., & Cahalan, J. H. (1992). A preliminary evaluation of wave attenuation
713 by four species of Seagrass. *Estuarine, Coastal and Shelf Science*, 35(6), 565-
714 576.

715 Fonseca, M. S., & Koehl, M. A. R. (2006). Flow in seagrass canopies: The influence of
716 patch width, *Estuarine, Coastal and Shelf Science* 67, 1-9.
717 doi:10.1016/j.ecss.2005.09.018
718

719 Folkard, A. M. (2005). Hydrodynamics of model *Posidonia oceanica* patches in shallow
720 water. *Limnology and Oceanography*. 50, 1592-1600.
721

722 Ghaitanellis, A., Violeau, D., Ferrand, M., El Kadi Abderrezak, K., Leroy, A., & Joly
723 A. (2018). A sph elastic-viscoplastic model for granular flows and bed-load
724 transport. *Advances in Water Resources*, 111, 156–173.
725

726 Ghisalberti, M., & Nepf, H. (2002). Mixing layers and coherent structures in vegetated
727 aquatic flows. *J. Geophys. Res.*, 107(C2). doi:10.1029/2001JC000871.
728

729 Gingold, R. A., & Monaghan, J. J. (1977). Smoothed particle hydrodynamics: theory
730 and application to non-spherical stars. *Mon. Not. R. Astron. Soc.*, 181, 375–389.
731

732 Gómez-Gesteira, M., Rogers, B. D., Dalrymple, R. A., Crespo A.J.C., &
733 Narayanaswamy, M. (2010). User Guide for the SPHysics Code v2.0.
734 <http://wiki.manchester.ac.uk/sphysics>
735

736 Gotoh, H., & Khayyer, A. (2018). On the state-of-the-art of particle methods for coastal
737 and ocean engineering. *Coastal Engineering Journal*, 60(1), 79-103. doi:
738 [10.1080/21664250.2018.1436243](https://doi.org/10.1080/21664250.2018.1436243)
739

740 Gray, J. P., Monaghan, J. J., & Swift, R. P. (2001). SPH elastic dynamics. *Comp*
741 *Methods Appl Mech Eng.*, 190, 6641-6662.
742

743 Ha, Y. D., Kim, M. G., Kim, H. S., & Cho, S. (2011). Shape design optimization of
744 SPH fluid–structure interactions considering geometrically exact interfaces.
745 *Struct Multidisc Optim*, 44, 319–336.
746

747 Hérault, A., Bilotta, G., & Dalrymple, R. A. (2010). SPH on GPU with CUDA. *J. Hydr.*
748 *Res.*, 48 (Extra Issue), 74-79.
749

750 Hérault, A., Bilotta, G., Dalrymple, R. A., Rustico, E., & Del Negro, C. (2011).
751 GPUSPH (Version 2.0) (Software) Available from
752 www.ce.jhu.edu/dalrymple/GPUSPH
753

754 Hérault, A., Bilotta, G., Dalrymple, R. A. (2014), Atteindre la meilleure précision dans
755 une mise en œuvre SPH. *Proc. 9th SPHERIC Int. Atelier, Paris (France)*, 134-
756 139.
757

758 Hervouet, J.-M. (2007). *Hydrodynamics of Free Surface Flows, Modelling with the*
759 *Finite element Method*. John Wiley & Sons Ltd., West Sussex, England.
760

761 Kajtar, J., & Monaghan, J. J. (2008). SPH simulations of swimming linked bodies [J].
762 *Journal of Computational Physics*, 227(19), 8568-8587.
763

764 Kazemi, E., Koll, K., Tait, S., & Shao S. (2020). SPH modelling of turbulent open
765 channel flow over and within natural gravel beds with rough interfacial
766 boundaries, *Advances in Water Resources*, 140.
767

768 Kobayashi, N., Raichlen, A. W., & Asano, T. (1993). Wave Attenuation by Vegetation.
769 *Journal of Waterway, Port, Coastal, and Ocean Engineering*, 119(1), 30-48.
770

771 Koftis, T., Prinos, P., & Stratigaki, V. (2013). Wave damping over artificial Posidonia
772 oceanica meadow: A large-scale experimental study, *Coastal Engineering* (73),
773 71-83. doi:10.1016/j.coastaleng.2012.10.007

774 Le Bouteiller, C., & Venditti, J. G. (2015). Sediment transport and shear stress
775 partitioning in a vegetated flow. *Water Resour. Res.*, 51, 2901–2922.
776 doi:10.1002/2014WR015825
777

778 Le Tallec, P., & Mouro, J. (2001). Fluid structure interaction with large structural
779 displacements. *Computer Methods in Applied Mechanics and Engineering*,
780 190(24–25), 3039-3067. doi: 10.1016/S0045-7825(00)00381-9
781

782 Liang, D., Jian, W., Shao, S., Chen, R., & Yang, K. (2017). Incompressible SPH
783 Simulation of Solitary Wave Interaction with Movable Seawalls. *Journal of*
784 *Fluids and Structures* 69, 72–88. doi:10.1016/j.jfluidstructs.2016.11.015
785

786 Liu, G. R. (2002). *Mesh Free methods: Moving beyond the finite element method*. CRC
787 Press, Boca Raton.

788 Luettich, R.A., Jr., Westerink, J.J., & Scheffner, N.W. (1992). ADCIRC: an advanced
789 three-dimensional circulation model for shelves coasts and estuaries, report 1:
790 theory and methodology of ADCIRC-2DDI and ADCIRC-3DL, Dredging
791 Research Program Technical Report DRP-92-6, U.S. Army Engineers
792 Waterways Experiment Station, Vicksburg, MS, 137p.

793 Lucy, L. B. (1977). A numerical approach to the testing of the fission hypothesis.
794 *Astron. J.*, 82, 1013–1024.

795

796 Luhar, M., & Nepf, H. (2011). Flow-induced reconfiguration of buoyant and flexible
797 aquatic vegetation. *J of Limnology and Oceanography*, 56(1), 2003-2017.

798

799 Madsen, J. D., Chambers, P. A., James, W. F., Koch, E. W., & Westlake, D. F. (2001).
800 The interaction between water movement, sediment dynamics and submersed
801 macrophytes. *Hydrobiologia* 444, 71–84.

802

803 Mendez, F. J., & Losada, I. J. (2004). An empirical model to estimate the propagation of
804 random breaking and nonbreaking waves over vegetation fields. *Coastal*
805 *Engineering*, 51(2), 103-118.

806

807 Monaghan, J. J. (1982). Why particle methods work. *Siam J. Sci. Stat. Comput.* 3, 422-
808 433.

809

810 Monaghan, J. J., & Gingold, R.A. (1983). Shock simulation by the particle method
811 SPH. *J. Comp. Phys.* 52, 374-389.
812

813 Monaghan, J. J. (1989). On the problem of penetration in particle methods. *J.*
814 *Computational Physics*, 82, 1-15.
815

816 Monaghan, J. J. (1992). Smoothed particle hydrodynamics. *Annual Rev. Astron. Appl.*,
817 30, 543- 574.
818

819 Monaghan, J. J. (1994). Simulating free surface flows with SPH. *Journal*
820 *Computational Physics*, 110, 399- 406.
821

822 Monaghan, J. J., & Kocharyan, A. (1995). SPH simulation of multi-phase flow.
823 *Computer Physics Communication*, 87, 225-235.
824

825 Monaghan, J. J., Cas, R. A. F., Kos, A. M., & Hallworth, M. (1999). Gravity currents
826 descending a ramp in a stratified tank. *J. Fluid Mech.*, 379, 39–69.
827

828 Monaghan, J. J. (2005). Smoothed Particle Hydrodynamics. *Rep. Prog. Phys.* 68, 1703-
829 1759.
830

831 Morris, J. P., Fox, P. J., & Zhu, Y. (1997). Modeling low Reynolds number
832 incompressible flows using SPH. *J. Comp. Phys.* 136, 214-226.
833

834 Oudart, T., & Larroudé, Ph. (2012). SPH model to simulate movement of grass meadow
835 of Posidonia under waves. *Proceedings of 33rd International Conference on*
836 *Coastal Engineering*, 802–813.

837

838 Oudart, T., Larroudé, Ph., & Bouchette, F. (2013). Two numerical approaches: 2D and
839 3D SPH model to simulate extreme waves over a barrier island. *Journal of*
840 *Coastal Research, Special Issue 65*, 362-367.

841

842 Paquier, A., Meulé, S., Anthony, E. J., Larroudé, Ph., & Bernard, G. (2019). Wind-
843 Induced Hydrodynamic Interactions With Aquatic Vegetation in a Fetch-Limited
844 Setting: Implications for Coastal Sedimentation and Protection. *Estuaries and*
845 *Coasts* 42, 688–707. doi: 10.1007/s12237-018-00487-w

846

847 Paul, M., & Amos, C. L. (2011). Spatial and seasonal variation in wave attenuation over
848 *Zostera noltii*. *J. Geophys. Res.* 116, C08019. doi:10.1029/2010JC006797.

849

850 Peterson, B. C., Waldbieser, G. C., Bilodeau, L. (2004). IGF-I and IGF-II mRNA
851 expression in slow and fast growing families of USDA103 channel catfish
852 (*Ictalurus punctatus*). *Comparative Biochemistry and Physiology, Part A* 139,
853 317-323. doi : 10.1016/j.cbpb.2004.09.015

854

855 Randles, P.W., & Libersky, L.D. (1996). Smoothed particle hydrodynamics: some
856 recent improvements and applications. *Computer Methods in Applied Mechanics*
857 *and Engineering*, 139(1–4), 375-408.

858

859 Roelvink, D., Reniers, A., van Dongeren, A., van Thiel de Vries, J., McCall, R., &
860 Lescinski, J. (2009). Modelling storm impacts on beaches, dunes and barrier
861 islands. *Coastal Engineering*, 56(11–12), 1133–1152.

862

863 Rugonyi, S., & Bathe, K.J. (2001). On finite element analysis of fluid flows fully
864 coupled with structural interactions. *Comput Model Eng Sci.*, 2, 195–212.

865

866 Sánchez-González, J.F., Sánchez-Rojas, V., & Memos, C.D. (2011). Wave attenuation
867 due to *Posidonia oceanica* meadows. *Journal of Hydraulic Research Vol. 49(4)*,
868 503-514. doi : 10.1080/00221686.2011.552464

869 Stratigaki, V., Manca, E., Prinos, P., Losada, I.J., Lara, J.L., Sclavo, M., Amos, C.L.,
870 Cáceres, I., & Sánchez-Arcilla, A. (2011). Large-scale experiments on wave
871 propagation over *Posidonia oceanica*. *Journal of Hydraulic Research*, 49, 31-43.

872

873 Van Liedekerke, P., Odenthal, T., Smeets, B., & Ramon, H. (2013). Solving
874 microscopic flow problems using Stokes equations in SPH. *Computer Physics*
875 *Communications* 184(7). doi : 10.1016/j.cpc.2013.02.013

876

877 Wallace, S., & Cox, R. (2000). Effects of Seagrass on Nearshore Current and Wave
878 Dynamics. *27th International Conference on Coastal Engineering, Coastal*
879 *Engineering, ISBN 0 7844 0549 2, ASCE, 4 Volumes*, 878-890.

880

881 Waycott, M., Duarte, C., Carruthers, T., Orth, R., Dennison, W., Olyarnik, S.,
882 Calladine, A., Fourqurean, J., Heck, Jr., K., Randall Hughes, A., Kendrick, G.,
883 Judson Kenworthy, W., Short, F., & Williams, S. (2009). Accelerating loss of

884 seagrasses across the globe threatens coastal ecosystems. *PNAS*, *106* (30).
885 12377–12381. doi: 10.1073/pnas.0905620106
886
887 Widdows, J., Pope, N. D., Brinsley, M. D., Asmus, H., & Asmus, R. M. (2008). Effects
888 of seagrass beds (*Zostera noltii* and *Z. marina*) on near-bed hydrodynamics and
889 sediment resuspension. *Mar. Ecol. Prog. Ser.* *358*, 125–136.
890 doi:10.3354/meps07338
891
892 Zhang, A., Sun, P., Ming, F., & Colagrossi, A. (2017). Smoothed particle
893 hydrodynamics and its applications in fluid-structure interactions. *Journal of*
894 *Hydrodynamics*, *29*(2), 187-216. doi: 10.1016/S1001-6058(16)60730-8
895
896
897
898
899
900
901
902
903
904
905
906
907
908
909
910

911 List of Figures

912

913 **Fig. 1.** a) Set up of the plate, b) example of high deformation in a longer plate, and c)

914 schema of interaction.

915

916 **Fig. 2.** Comparison between the 3D numerical simulation and the theoretical vertical

917 displacement of the free end of the plate (case for a sinusoidal oscillation).

918 **Fig. 3.** Comparison between numerically simulated (sim) and experimental (exp)
919 displacements (a) vertical, and (b) horizontal) of the free end of the plate: Antoci et al.'s
920 (2007) experiment (black dots) and the current simulations with the Lennard-Jones
921 (Monaghan, 2005) formulation (LJ, stars) and with the Kajtar and Monaghan (2008)
922 formulation (MK, black squares), with an initial spacing between elastic particles 10
923 times smaller than the fluid particles with interface particles in the Kajtar and
924 Monaghan (2008) formulation (MK10, shown as a solid line).

925

926 **Fig. 4.** Seagrass meadow of *Posidonia Oceanica* (left) and (right) schematic SPH
927 discretization of water (blue) and seagrass meadow (green).

928

929 **Fig. 5.** Movement of three plants under a breaking wave using FSI simulated with SPH.

930

931 **Fig. 6.** Comparison between the experiment with artificial plants made of foam in Luhar
932 and Nepf (2011) and the current simulation following the third FSI SPH approach
933 presented in the study: a) set up of the experiment, b) simulation, and c) experiment
934 with current velocity $U=0.16$ m/s, d) simulation, and e) experiment with current velocity
935 $U=0.32$ m/s

936

937 **Fig. 7.** Wave height relative to the reference water level in the channel ($h_0 = 0.2$ m) as a
938 function of the cross-shore position for an h_0/h_{plant} ratio equal to 0.5. The vertical green
939 line shows the plant's position at $x = 1.2$ m (one plant). In the simulation with three
940 plants, they were located at $x = 1$, $x = 1.2$, and $x = 1.4$ m.

941

942 **Fig. 8.** Movement of the sea grass meadow under waves at different depths: a) with one
943 meadow of 200 plants, and b) with two separate meadows.

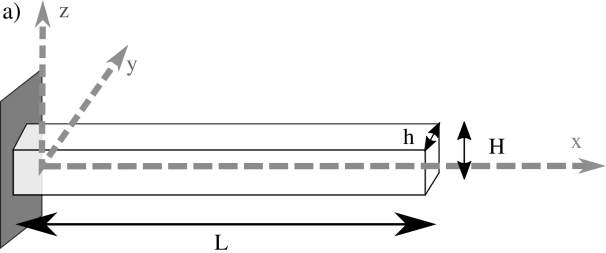
944

945 **Fig. 9.** GPUSPH 3D simulation of the real bathymetry in the Berre Lagoon: a), b) and c)
946 at 3 different times under one and the same wave, and d) simulated wave height with
947 and without plants using real off-shore wave height, beach bathymetry, and seagrass
948 zones

949

950 **Fig. 10.** Flume experiment done at the River Dynamics Laboratory at Simon Fraser
951 University, courtesy C. Le Bouteiller a) sketch of the experimental set up (figure from
952 Le Bouteiller & Venditti, 2015) where Q_w is the water discharge, Q_s is the sediment
953 transport rate, SMS is the Swath Mapping System, ADV is the Acoustic Doppler
954 Velocimetry, and SS sampling is the Seatek bed Sensors, b) photograph of the blades
955 during the experiment, c) close up of the numerical blades, and d) numerical flume at
956 the same dimensions as in the experiment, i.e. with a 4-m-long meadow

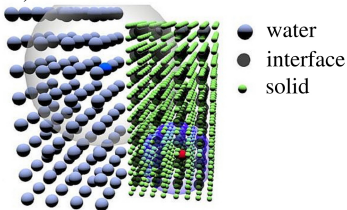
957

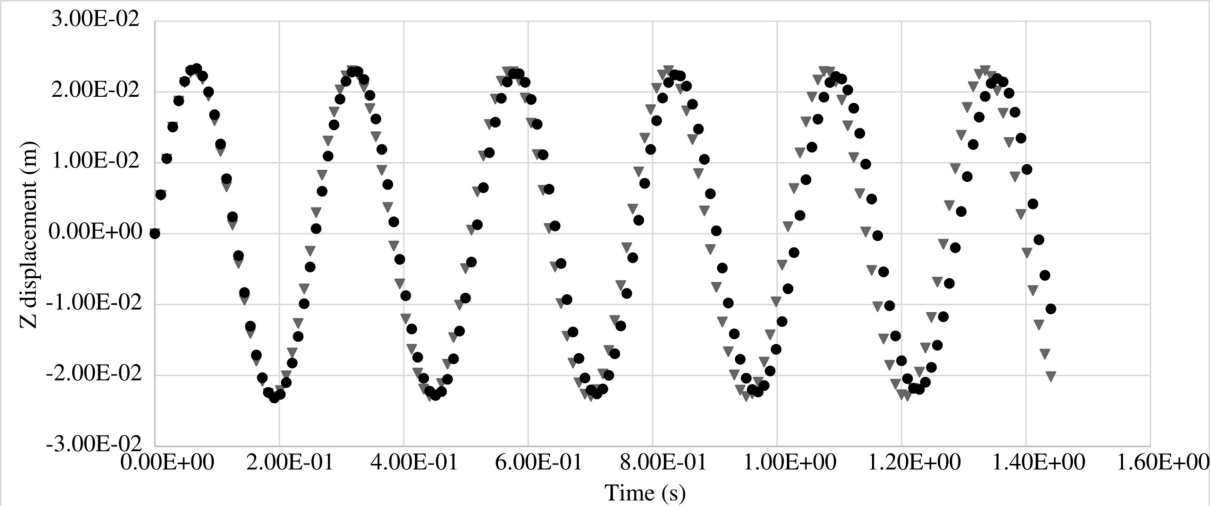


b)



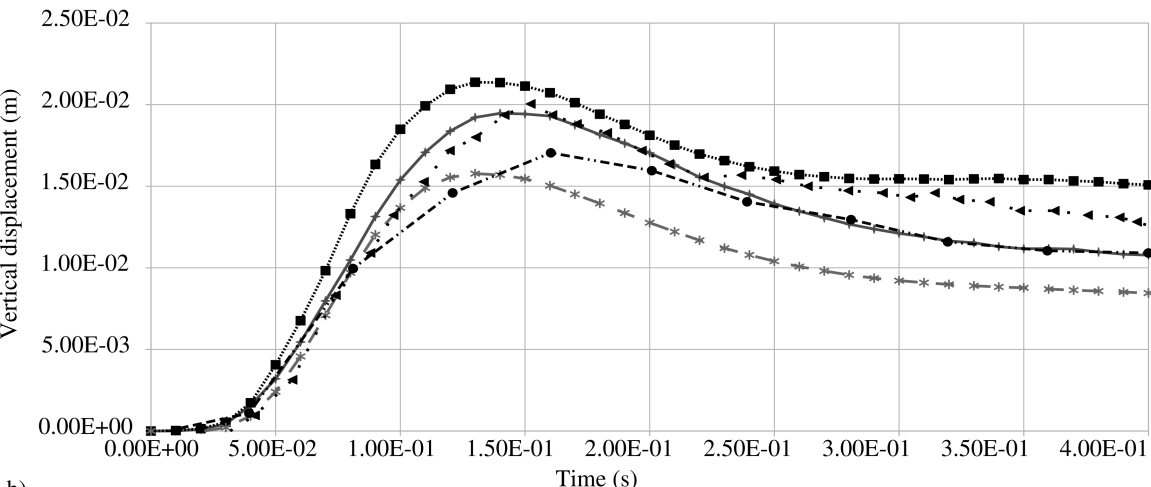
c)



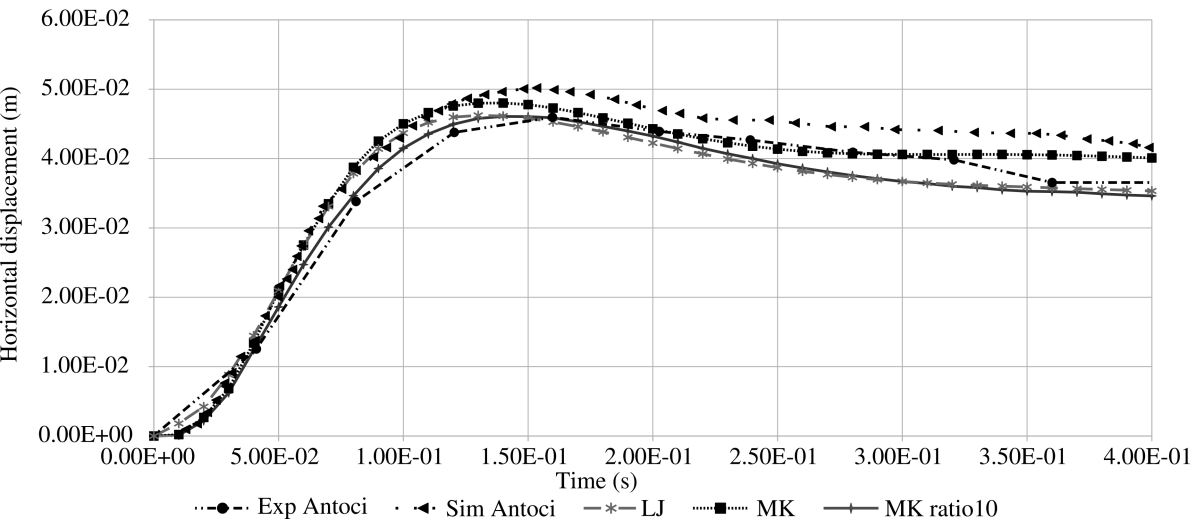


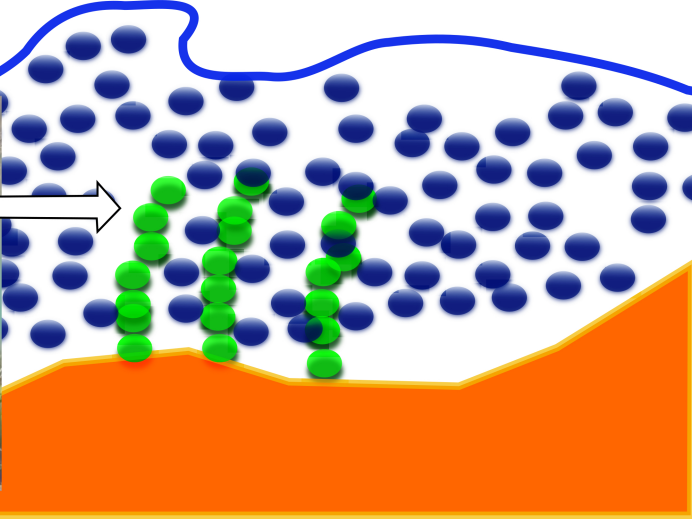
● Numerical ▼ Theoretical

a)

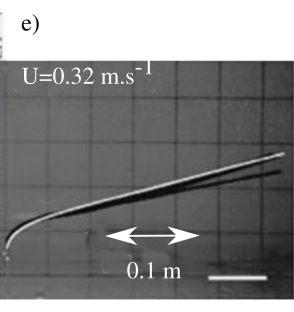
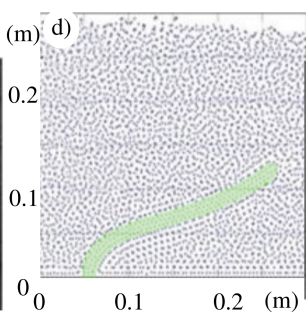
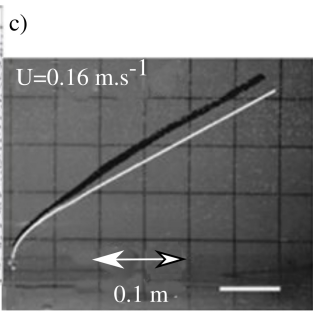
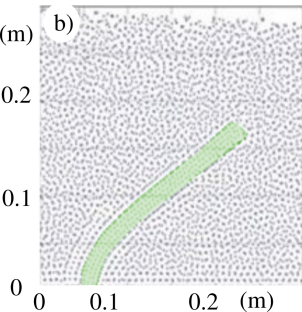
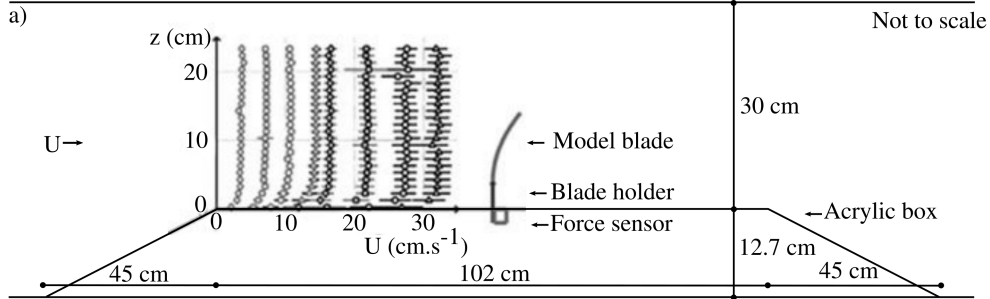


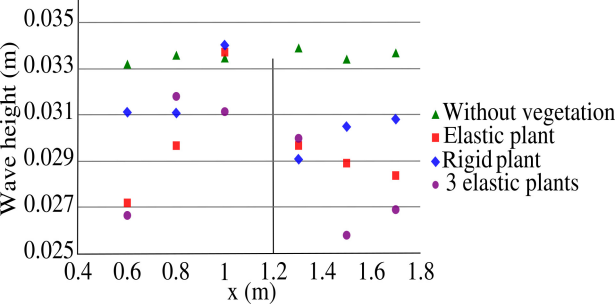
b)

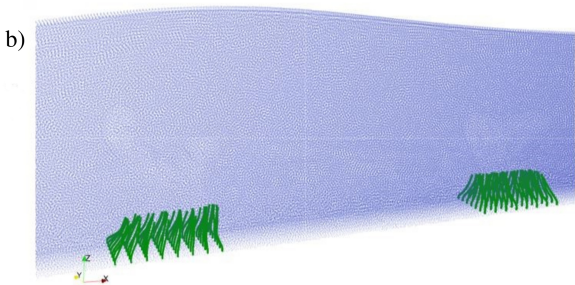
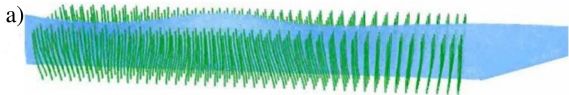


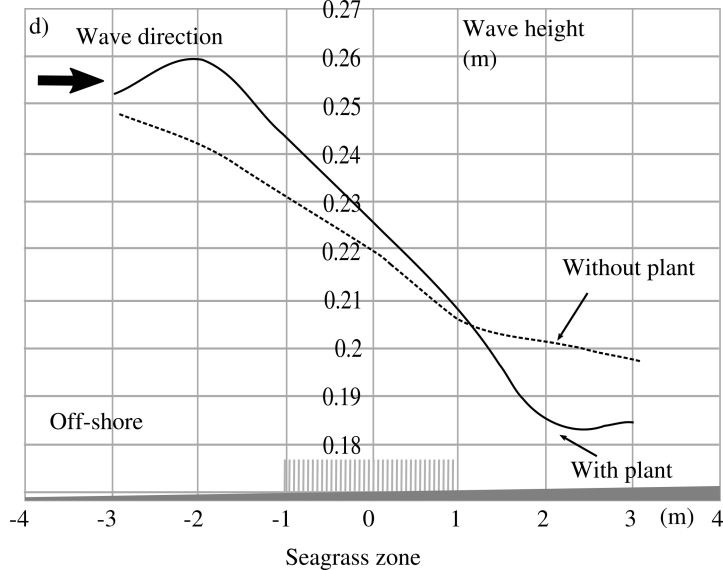
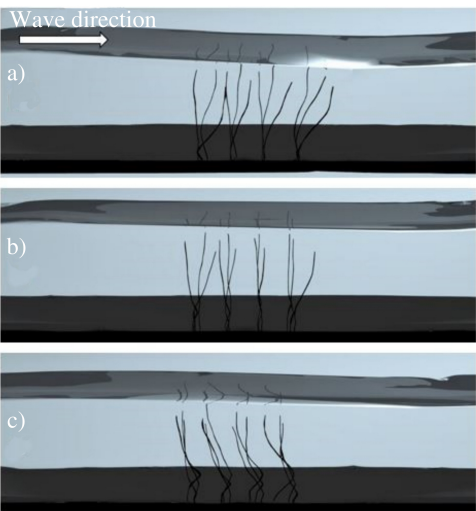












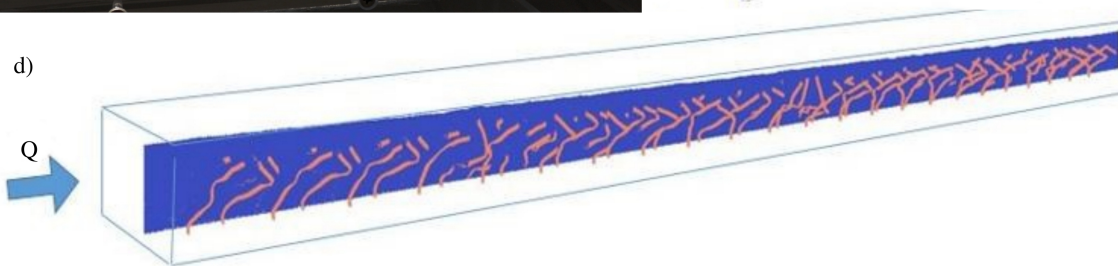
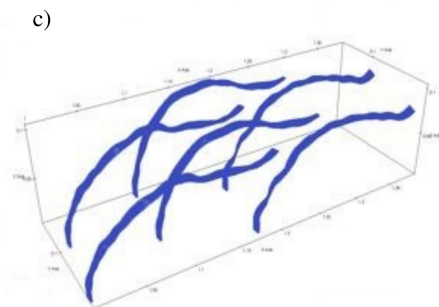
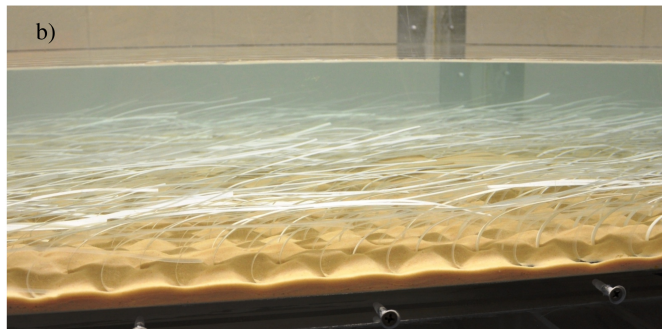
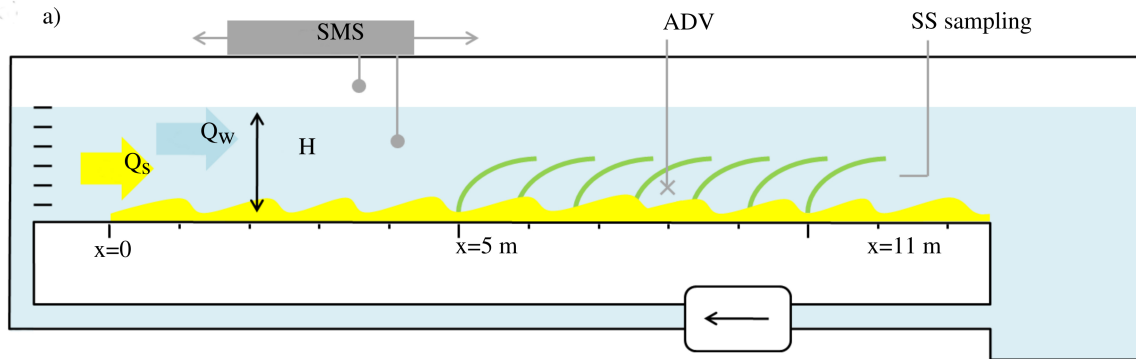


Table 1. Dimensions in the experiment.

Dimensions in the experiment	
A(m)	0.1
H(m)	0.14
B(m)	0.1
B*(m)	0.098
L(m)	0.079
s(m)	0.005

Table 2. Fluid and solid properties and elastic modulus used

Fluid properties	
Density, $\rho(\text{kg/m}^3)$	1,000
Compressibility modulus, ε (N/m^2)	2×10^6
Solid properties	
Density, ρ_s (kg/m^3)	1,100
Young's modulus, E (N/m^2)	1.2×10^7
Shear's modulus, μ (N/m^2)	4.27×10^6
Bulk modulus, K (N/m^2)	2×10^7

Table 3. Properties of real *Posidonia Oceanica* and modified properties used for numerical simulations, from (Folkard, 2005)

Property	Real Plant	Simulated Plant
Density, ρ_s (kg/m ³)	910 ± 110 kg/m ³	910 kg/m ³
Young's modulus, E (N/m ²)	$4.7 \pm 0.6 \times 10^8$ N/m ²	2.1×10^4 N/m ²
Thickness (mm)	0.1 mm	15 mm
Bulk modulus, K (N/m ²)	$3.92 \pm 0.6 \times 10^8$ N/m ²	1.7×10^4 N/m ²
Shear's modulus, μ (N/m ²)	$1.81 \pm 0.5 \times 10^8$ N/m ²	8.7×10^3 N/m ²